



Minerva Access is the Institutional Repository of The University of Melbourne

Author/s:

Sun, D;Shaik, NEK;Unnithan, RR;French, C

Title:

Hippocampal cognitive and relational map paradigms explored by multisensory encoding recording with wide-field calcium imaging

Date:

2024-01-19

Citation:

Sun, D., Shaik, N. E. K., Unnithan, R. R. & French, C. (2024). Hippocampal cognitive and relational map paradigms explored by multisensory encoding recording with wide-field calcium imaging. *Iscience*, 27 (1), <https://doi.org/10.1016/j.isci.2023.108603>.

Persistent Link:

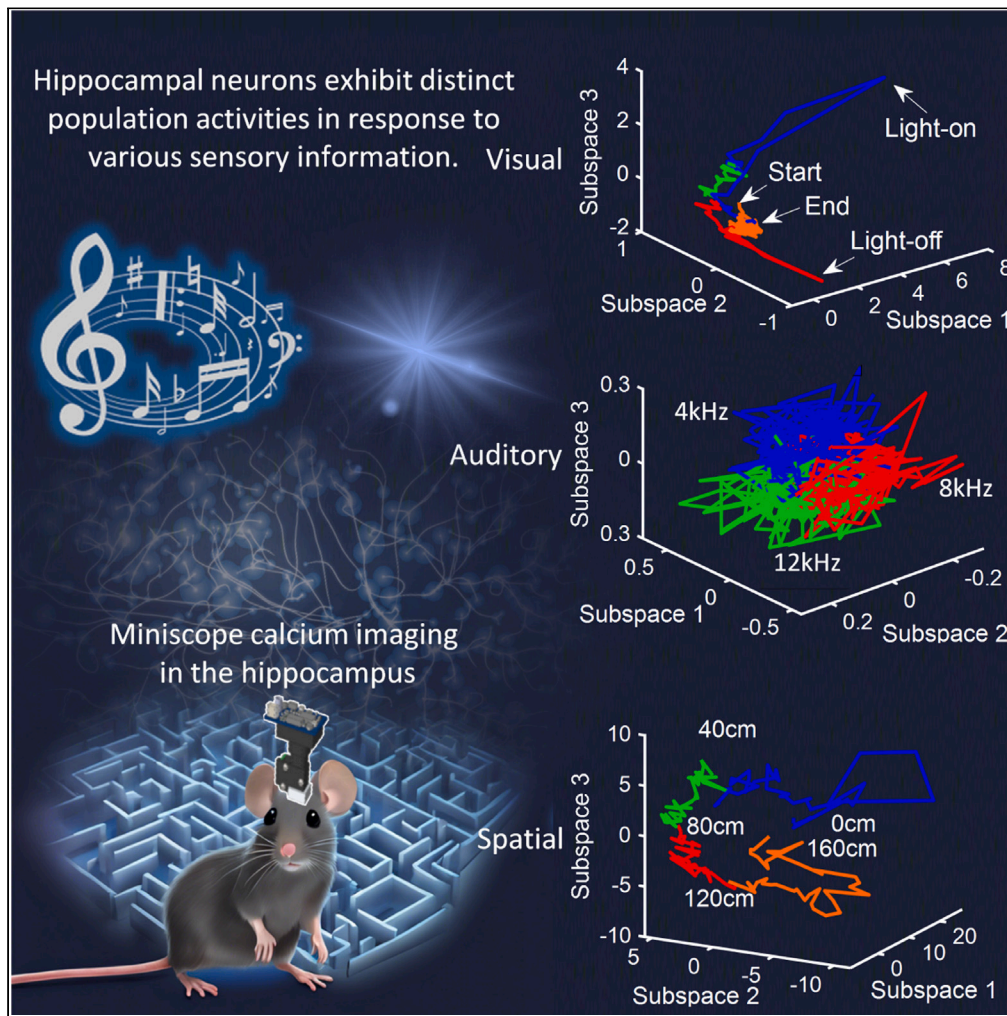
<https://hdl.handle.net/11343/344378>

License:

[CC BY-NC-ND](#)

Article

Hippocampal cognitive and relational map paradigms explored by multisensory encoding recording with wide-field calcium imaging



Dechuan Sun,
Noor E. Karishma
Shaik, Ranjith
Rajasekharan
Unnithan, Chris
French

dechuan.sun@unimelb.edu.au
(D.S.)
frenchc@unimelb.edu.au (C.F.)

Highlights

The hippocampus can process non-spatial information independently

Hippocampal multisensory encoding supports the relational theory

Non-spatial stimuli induce topological changes in the hippocampal neural network

The hippocampus processes sensory information through various mechanisms

Sun et al., iScience 27, 108603
January 19, 2024 © 2023 The
Authors.
[https://doi.org/10.1016/
j.isci.2023.108603](https://doi.org/10.1016/j.isci.2023.108603)

Article

Hippocampal cognitive and relational map paradigms explored by multisensory encoding recording with wide-field calcium imaging

Dechuan Sun,^{1,2,*} Noor E. Karishma Shaik,² Ranjith Rajasekharan Unnithan,² and Chris French^{1,3,*}

SUMMARY

Two major theories have been proposed to explain hippocampal function: cognitive map and the relational theories. They differ in their views on whether hippocampal neurons can process non-spatial information independently. However, the explanatory power of these theories remains unresolved. Additionally, more complex aspects of hippocampal neural population responses to non-spatial stimuli have not been investigated. Here, we used miniaturized fluorescence microscopy to investigate mouse CA1 responses to spatial, visual, auditory modalities, and combinations. We found that while neuronal populations primarily processed spatial information, they also showed strong sensitivity to non-spatial modalities independent of spatial inputs, exhibiting distinct neuronal dynamics and coding patterns. These results provide strong support for the relational theories.

INTRODUCTION

The hippocampus plays a crucial role in memory, navigation, and cognition.^{1–3} Previous studies have developed several theories of rodent hippocampal function, which can be divided into two distinct categories depending on the role assigned to spatial information processing. The influential *cognitive map* theory views spatial information as the primary organizational principle, while signals of other sensory modalities are integrated in a spatial framework as features for processing.^{4,5} In contrast, the *relational* theory proposes that the hippocampus supports a broader function with different types of information processed independently, and spatial representation is simply an example of a general mechanism for encoding information.^{1,6,7} It has been shown that non-spatial factors can modulate the activity of hippocampal neurons, such as olfactory, gustatory, tactile, auditory, and visual. However, these non-spatial responses have been found to be spatial context-dependent or task-dependent in almost all previous studies.⁵ Consequently, such responses may actually represent the location or context in which the feature is present rather than the feature per se, and in turn challenge the relational theory.

However, no experiments have been designed to exclude the interference of spatial information when studying non-spatial responses. It has become apparent that responses to salient stimuli are more adequately and stably represented by neural population activity compared with intrinsically variable single-neuron responses.⁸ Additionally, it has been reported that multidimensional population responses can be more effectively parsed using population-level analyses such as graph topological analyses or manifold analyses,^{9,10} which have not previously been employed for analysis of non-spatial information in CA1. Interestingly, it has recently been reported that rhythmic light stimulation can enhance memory function in a rodent model of Alzheimer's disease,¹¹ suggesting more complex roles for light stimulation beyond simple sensory detection and emphasizing the need for a more comprehensive understanding of hippocampal responses to non-spatial stimuli.

Since it is impossible to eliminate all spatial inputs to the animal, we placed the animal in a small recording chamber during the experiment. This arrangement was designed to minimize spatial influences, allowing the animal to be passively exposed to either visual stimuli, auditory stimuli at different frequencies, or a combination of both. Notably, stimuli were introduced randomly throughout the experiment, a factor that significantly reduced the interference of spatial inputs, because if neuronal responses do indeed represent feature-in-place responses, consistent stimuli-evoked neuronal firing patterns should not be detectable. Additionally, we observed the population activity when animals traversed a linear track. The hippocampal calcium activity was recorded simultaneously using a miniaturized fluorescence microscope¹² ("miniscope", Figure 1). We first studied the properties of individual neuronal activity, and then topology connectivity and population activity using graph theory and manifold analysis, respectively. Additionally, we tested for critical dynamical behavior of neuronal populations over time to determine neural dynamic variation in response to repeated stimuli. We demonstrate that the hippocampus processes non-spatial information irrespective of spatial inputs. The network topology shows very dense connections for spatial information but quite sparse connections for non-spatial information, and neuronal populations displayed different coding mechanisms depending on sensory inputs. The neuronal system moves away from the critical state over time in visual and auditory stimuli experiments but remained stable in mixed stimuli

¹Neural Dynamics Laboratory, Department of Medicine, The University of Melbourne, Melbourne, VIC, Australia

²Department of Electrical and Electronic Engineering, The University of Melbourne, Melbourne, VIC, Australia

³Lead contact

*Correspondence: dechuan.sun@unimelb.edu.au (D.S.), frenchc@unimelb.edu.au (C.F.)

<https://doi.org/10.1016/j.isci.2023.108603>



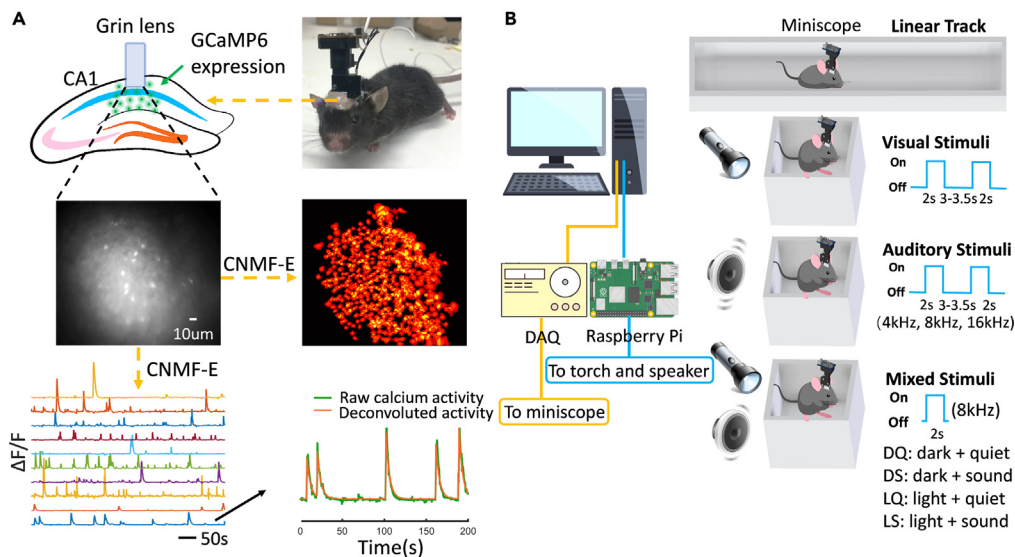


Figure 1. Hippocampal calcium activity and experimental design

(A) A Grin lens was implanted into the hippocampal CA1 to observe the calcium activity of GCaMP6 virus-labeled neurons. The CNMF-E algorithm was used to identify spatial footprints of detected neurons, and the raw calcium activity was deconvoluted to get the calcium event signal.

(B) Experimental design. The animal's brain activity was studied in four separate experiments: (1) mice traversed a linear track; mice were exposed to either (2) light stimuli or (3) sound stimuli at different frequencies or (4) light-sound mixed stimuli. The torch and speaker were controlled using a Raspberry Pi board that was synchronized with the miniscope recording system.

experiments. Together, these results enhance our understanding of hippocampal neuronal population activity in response to various modalities of information and provide support for the relational theory.

RESULTS

Hippocampal neural activity was studied in four separate experimental scenarios: light stimuli, sound stimuli, linear track, and light-sound mixed stimuli. We analyzed both the neuronal firing patterns of each individual neuron and the population activity. The initial part of our analysis primarily focused on assessing the informational characteristics of each neuron's firing pattern. Information content was used to quantify the amount of information encoded within neuronal firing patterns, aiding in the evaluation of neural coding complexity. Additionally, we measured the cosine similarity index to evaluate the stability of these firing patterns across trials. We also examined the information-similarity joint density distribution to understand the spatial distribution of information and similarities. Furthermore, mutual information was measured to assess the statistical dependencies between different stimuli and to evaluate the flow of information. Finally, we utilized a machine-learning-based autoencoder method to uncover hidden deep features within the neuronal firing patterns of each neuron. The second part of the analysis focused on population activity. Graph theory modeled complex connectivity and interactions between neuronal populations in the network, while manifold analysis explored high-dimensional neuronal data structures to identify underlying population firing patterns. Criticality analysis provided insights into neural network stability and adaptability. The comparison of the results in different experiments will be elaborated later in the [discussion](#) section.

Neural representation during light exposure

To explore the light sensitivity of hippocampal neuronal ensembles, we studied hippocampal calcium activity when mice ($n = 5$) were exposed to repeated light stimuli as described in the methods. Many neurons displayed clear stimuli-evoked responses, especially during dark-to-light ($13.65\% \pm 1.92\%$) and light-to-dark transients ($23.08\% \pm 5.47\%$; [Figure 2A](#)). We then investigated the resulting neural activity in four temporal windows: 15 frames before and after time point 0 (DL: dark-to-light transient), 1 (L: light), 2 (LD: light-to-dark transient), and 3 s (D: dark). To assess the neuronal coding precision, we measured the information content of each neuron in four temporal windows. Neurons in the DL window had much higher information content, suggesting a more complex and precise coding process ([Figures 2B and S1A](#)). We next measured the cosine similarity index of each neuron to evaluate the temporal stability of neural firing patterns. Patterns in DL and LD windows demonstrated very high stability, especially around the activation and cessation of the stimulus. In contrast, patterns in L and D windows displayed comparable low stability ([Figures 2C and S1B](#)). Given that both the information content and cosine similarity index were measured from each neuron, we tested whether these might be co-dependent by computing the joint density distribution and observed different distributions in four time windows ([Figures 2D and S1C](#)). To detect non-obvious activity patterns, we used an autoencoder to reduce the data dimensionality and extracted the most significant features. The autoencoder greatly improved discrimination, with clear distinctions detected even in L and D windows, where the previously described metrics did not reveal clear differences ([Figures 2E and S1D](#)). Examples of detected

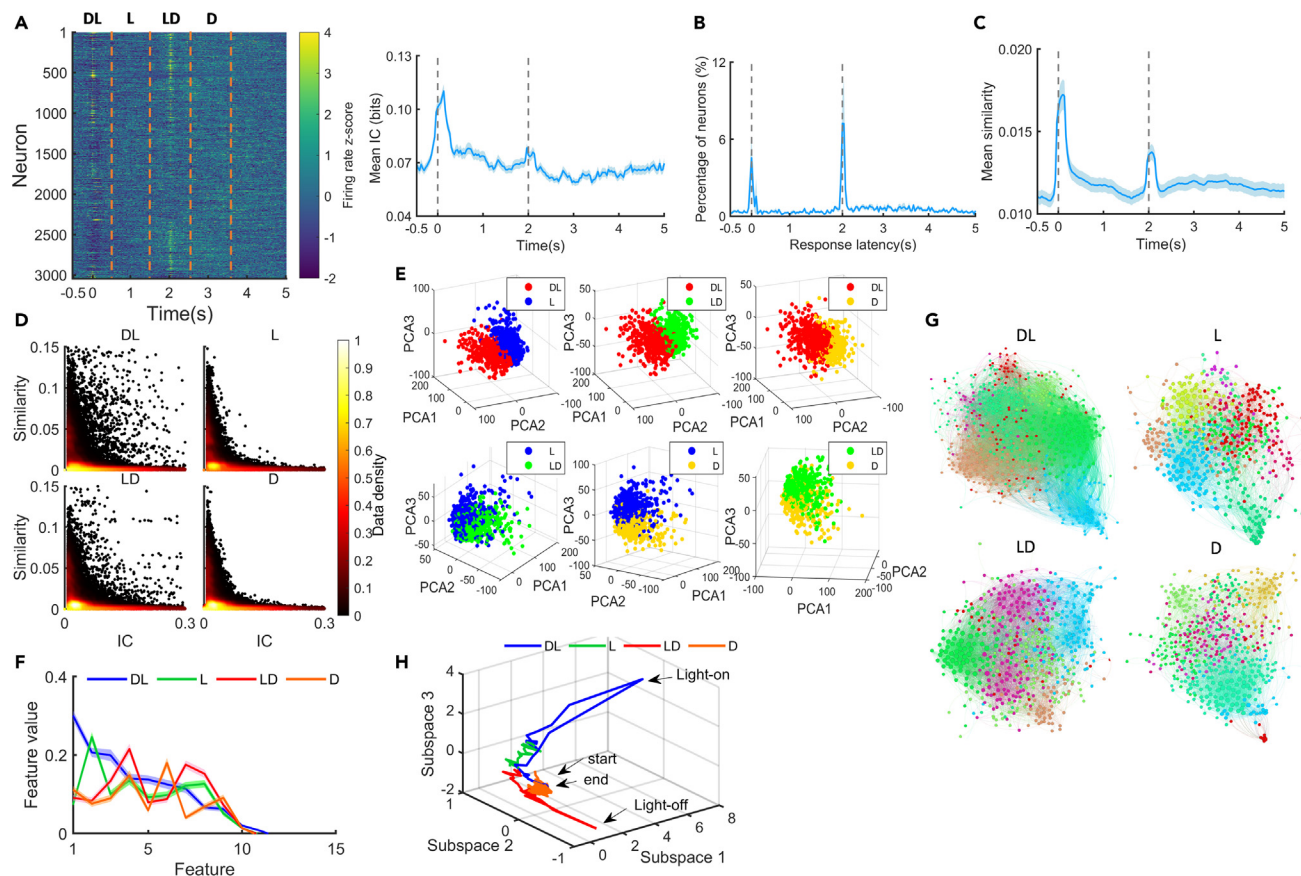


Figure 2. Both individual signal neurons and neuronal populations exhibited time-varying responses to visual stimuli

The flashlight was switched on at time $t = 0$ s and switched off at time $t = 2$ s. The activity was divided into four temporal windows for analysis: dark-to-light transient (DL), light (L), light-to-dark transient (LD), and dark (D).

(A) The average neuronal temporal firing rate map over trials and the distribution of neuronal response latencies.

(B) Neurons within the DL transient carried higher information content than others.

(C) The temporal neuronal firing patterns within DL and LD transients showed higher stability across trials when measured using the cosine similarity index.

(D) Information-similarity joint density distribution showed distinct patterns in different windows.

(E) Examples of neuronal firing patterns analyzed using an autoencoder. Each dot represents the firing pattern of a specific neuron. Since there were more than three extracted features, PCA was applied to the autoencoder results for better visualization.

(F) The average feature values, representing the most significant components of neuronal firing patterns detected using the autoencoder, were measured in different windows.

(G) Neuronal population in different windows showed different topology structure.

(H) An example of the neural manifolds representation.

features are shown in Figures 2F and S1E. We next measured the weighted normalized mutual information of each neuron between every two windows (DL-L, DL-LD, DL-D, L-LD, L-D, LD-D), and found that there were more sensitive neurons between transient periods and fewer between non-transient periods (Figures S2A–S2D). Additionally, weighted mutual information was also measured (Figure S2E).

Individual neurons exhibited clear stimuli-dependent firing patterns, but we sought to characterize the ensemble response as it is known that sets of neurons may encode salient properties in a more complex distributed pattern than evident from single neuronal responses. We therefore studied the topological connectivity and overall firing pattern of neuronal ensembles using graph theory and neural manifold analysis, respectively. We first measured correlation coefficients between neuron pairs and modeled neuronal population connectivity using graph theory (Figure S3A). Network graphs of correlated neural activity demonstrated a clear stimuli-dependent topology (Figure 2G). Compared to other windows, the network graph in the DL window had a denser structure, and there were more neurons showing stronger influence on the entire network (Figures S3B and S3C). The functional connectivity of the neuronal population varied, with neurons and cell groups in the DL window showing the highest clustering coefficient and more localized connectivity, respectively (Figure S3D). Significant connectivity differences were also detected between D and L windows (Figure S3E). We next studied overall population activity by seeking to identify neural manifolds. Cortical neuronal population activity displays redundancy in several systems, wherein multiple neuronal populations may exhibit analogous patterns of activity despite processing different types of information or performing different tasks. Thus, we reduced the dimensionality of the population activity

using a machine learning method (see [STAR Methods](#)). We found that the majority of the variation in neuronal population activity (first three most significant features derived from the autoencoder) was represented by an intrinsic low-dimensional neural manifold that appeared confined to a closed-loop “C-shape” geometry ([Figures 2H and S3F](#)). Manifold amplitudes and angles provide two ways to quantify the similarity between neural modes and indicate when self-similarity breaks down. Throughout the onset and offset of the stimulus, the activity in neural manifolds revealed a substantial deviation from the origin of the coordinate. Additionally, the activity during light exposure displayed much larger angles than that during the non-exposure period, revealing changes in self-similarity of neural modes ([Figure S3G](#)).

We next sought evidence for critical dynamical behavior, and its temporal stability. We split the recording session in half and tested the population activity for markers of critical dynamics in each half. The system did display properties of criticality that varied over time. The sizes and durations of neuronal avalanches in both periods followed power-law distributions ([Figures S4A and S4B](#)). Several other measures of critical behavior were also clearly demonstrated by the network behavior including the deviation from criticality coefficient (DCC) error, branching ratio (BR), and shape collapse error (SC), allowing more rigorous identification of critical behavior. The network moved away from the critical state as time passed, as measured by the increased DCC error and reduced BR ([Figures S4C and S4D](#)). However, the SC errors did not appear to change significantly ([Figure S4E](#)).

Neural representation of auditory stimuli

We next studied neural activity when mice ($n = 5$) were exposed to sound stimuli at three different frequencies. The signal was sectioned into three types of epochs according to the stimuli frequency (4, 8, and 16 kHz) for analysis. We found that some neurons activated immediately after the onset of stimuli (4 kHz: $3.72\% \pm 2.22\%$, 8 kHz: $3.54\% \pm 1.04\%$, 16 kHz: $5.61\% \pm 2.54\%$), whereas most neurons started firing with varying degrees of delays ([Figure 3A](#)). We then investigated coding properties of each neuron. Unlike visual stimuli experiments, neuronal information content remained comparatively stable over time without showing a surge with stimulus onset or offset. Compared to 4 and 16 kHz epochs, neurons in 8 kHz epochs displayed substantially higher information content ([Figures 3B and S5A](#)). Neuronal firing patterns remained temporally stable in 4 and 16 kHz epochs, with several neurons displaying strong stability immediately after stimulation. In contrast, the stability in 8 kHz epochs displayed a “U shape” pattern ([Figures 3C and S5B](#)). Additionally, the information-similarity density distribution differed between epochs ([Figures 3D and S5C](#)). An autoencoder was applied to reduce the data dimensionality and identify hidden activity patterns. With the autoencoder, neuronal firing patterns in different frequency epochs could be distinguished into different clusters, suggesting that the sound frequency was encoded using quite different temporal coding processes ([Figures 3E, 3F, S5D, and S5E](#)). Intriguingly, there were fewer sensitive neurons when comparing the neural activity between 4 and 16 kHz epochs, indicating heterogeneity of hippocampal neurons to sound frequencies ([Figure S6](#)).

We next characterized the neuronal population activity in response to sound and observed different frequency-dependent network topologies ([Figures 3G and S7A](#)). Compared to 8 kHz epochs, neurons in 4 kHz epochs displayed a higher tendency to cluster ([Figure S7D](#)). Additionally, cell groups in 4 kHz epochs showed the strongest localized connectivity ([Figure S7E](#)). We also studied and compared the network density and the influence of each neuron to the network, but no significant differences were found with frequency ([Figures S7B and S7C](#)). In contrast to the visual stimuli findings, the neural manifold representing auditory frequency appeared to have a very “chaotic” geometry, but with each frequency confined to a separate subregion ([Figure 3H](#)). Population activity varied between scenarios, with manifold activity showing different angles. However, the manifold amplitude displayed quite similar patterns ([Figures S7F–S7H](#)).

We then characterized criticality parameters of neuronal populations in the first half and the second half of the experiment. Again, the sizes and durations of neuronal avalanches in both periods were well approximated by truncated power-law distributions ([Figures S8A and S8B](#)). However, the DCC error significantly increased over time ([Figures S8C–S8E](#)), suggesting that the network gradually tuned away from the critical state over the period of observation.

Neural representation during linear track experiments

Non-spatial stimuli alter the characteristics of hippocampal CA1 neuronal ensembles. How do population activity and network topology change with spatial inputs? We next studied ensemble CA1 neural activity when well-trained mice ($n = 5$) traversed a linear track. The signal was divided into several 1 cm spatial bins, and we recorded neural responses in four long segments: spatial bins 1–40 (S1), 41–80 (S2), 81–120 (S3), and 121–160 (S4). Several neurons exhibited high information contents, particularly at both ends of the track ([Figure 4A](#)). Nonetheless, the stability of neuronal firing patterns was very low at both ends. On average, neurons in S4 had the lowest information content, but the highest stability ([Figures 4B, 4C, S9A, and S9B](#)). In contrast to the visual and auditory stimuli experiments, information-similarity density distributions in the four scenarios exhibited quite similar patterns ([Figures 4D and S9C](#)). However, after applying an autoencoder to extract significant features, activity in different segments could be separated into different clusters ([Figures 4E, 4F, S9D, and S9E](#)). Neurons showed different sensitivity in the four spatial segments. There were more sensitive neurons when comparing the activity between S1 and S4, and less sensitive neurons between S2 and S3 ([Figure S10](#)).

We next studied the topology structure and properties of neuronal population activity for spatial orientation. In comparison to non-spatial stimuli experiments, neuronal ensembles showed much more synchronized activity. Different topologies were observed in each spatial segment ([Figures 4G and S11A](#)). Specifically, neurons in S1 and S4 showed considerably denser structure and stronger influence on the network than neurons in S2 and S3 ([Figures S11B and S11C](#)). Additionally, neurons in S1 and S4 exhibited substantially higher clustering coefficients, whereas cell groups displayed more localized connectivity ([Figures S11D and S11E](#)). Additionally, the population activity was projected to a low-dimensional subspace by employing neural manifold analysis. Different population dynamics were observed in the four spatial segments, with large manifold amplitudes in S1 and S4 ([Figures 4H, S11F, and S11G](#)). Additionally, the manifold angles displayed an “M” shape pattern ([Figure S11G](#)), with two peaks appearing in S1 and S4.

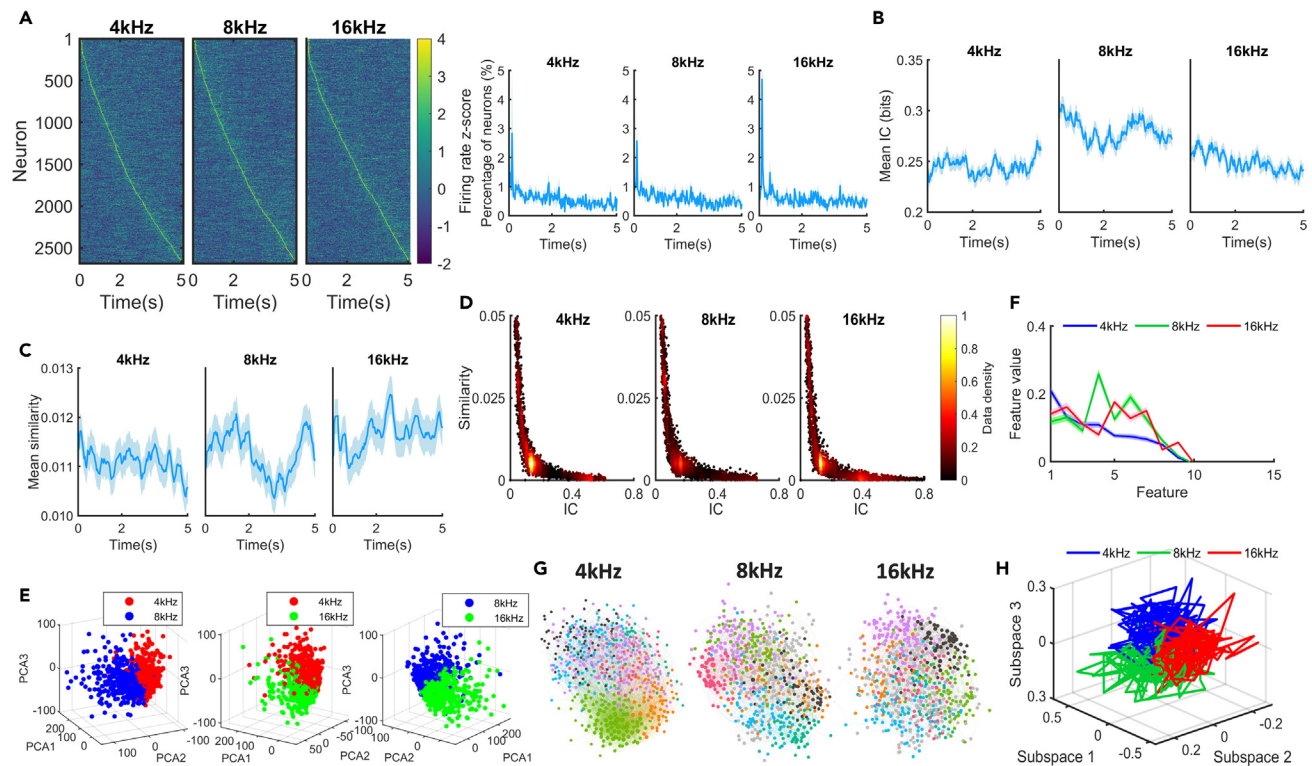


Figure 3. Distinct neuronal firing patterns were observed when the animal received auditory stimuli of different frequencies

The speaker was activated at time $t = 0$ s and deactivated at time $t = 2$ s. The activity was divided into three frequency epochs (4, 8, and 16 kHz) for analysis. (A) The average neuronal temporal firing rate map over trials in different frequency epochs. Neuronal populations exhibited widely distributed response latencies. (B) Neurons in 8 kHz epochs carried higher information content than in other epochs. (C) Neuronal firing patterns in 16 kHz epochs showed the highest stability when measured using the cosine similarity index while patterns in 4 kHz epochs showed the lowest stability. (D) Information-similarity joint density distribution showed distinct patterns in different windows. (E) Examples of neuronal firing patterns analyzed using an autoencoder. Each dot represents the firing pattern of a specific neuron. PCA was applied to results for better visualization. (F) Firing patterns in different windows exhibited varying average feature values. (G) Neuronal population in different windows showed different topology structure. (H) An example of the neural manifolds representation.

Criticality measures remained stable during the first half and the second half of the experiment although the SC error reduced significantly over time, suggesting configuration closer to the critical point (Figure S12). However, it is worth noting that SC is a noisier metric than others, precluding definite conclusions about the overall effect of these changes on system dynamics.

Neural representation during mixed light-sound stimuli

As we had shown sensitivity to non-spatial stimuli, we next examined how mixed non-spatial stimuli affect hippocampal CA1 neuronal activity by analyzing neuronal population activity when mice ($n = 5$) were exposed to mixed light-sound stimuli. The signal was sectioned into four different types of epochs in four environments (DQ: dark + quiet; DS: dark + sound; LQ: light + quiet; LS: light + sound). At the beginning of each epoch, a substantial proportion of neurons responded instantly to stimuli, but the quantity in DQ ($35.88\% \pm 6.63\%$) and DS ($36.27\% \pm 8.19\%$) epochs was much higher than that in LQ ($17.77\% \pm 4.65\%$) and LS ($21.79\% \pm 4.87\%$) epochs (Figure 5A). We next examined coding properties of each neuron. Intriguingly, similar temporal information content and cosine similarity index were observed between DQ and DS epochs and LQ and LS epochs, respectively. The information content was at a relatively high level at the beginning of each epoch, then reduced rapidly (DQ, DS) or gradually (LQ, LS) to a similar level. On average, the information content was higher in LQ and LS epochs than that in DQ and DS epochs (Figures 5B and S13A). The temporal stability of neuronal firing patterns decreased in all scenarios with a relatively high cosine similarity index at the beginning. Contrary to the information content result, neurons in DQ and DS epochs revealed substantially higher stability (Figures 5C and S13B). Again, similar information-similarity density distributions were observed between DQ and DS epochs and LQ and LS epochs, respectively (Figures 5D and S13C). Although there were no obvious changes in information content and stability of

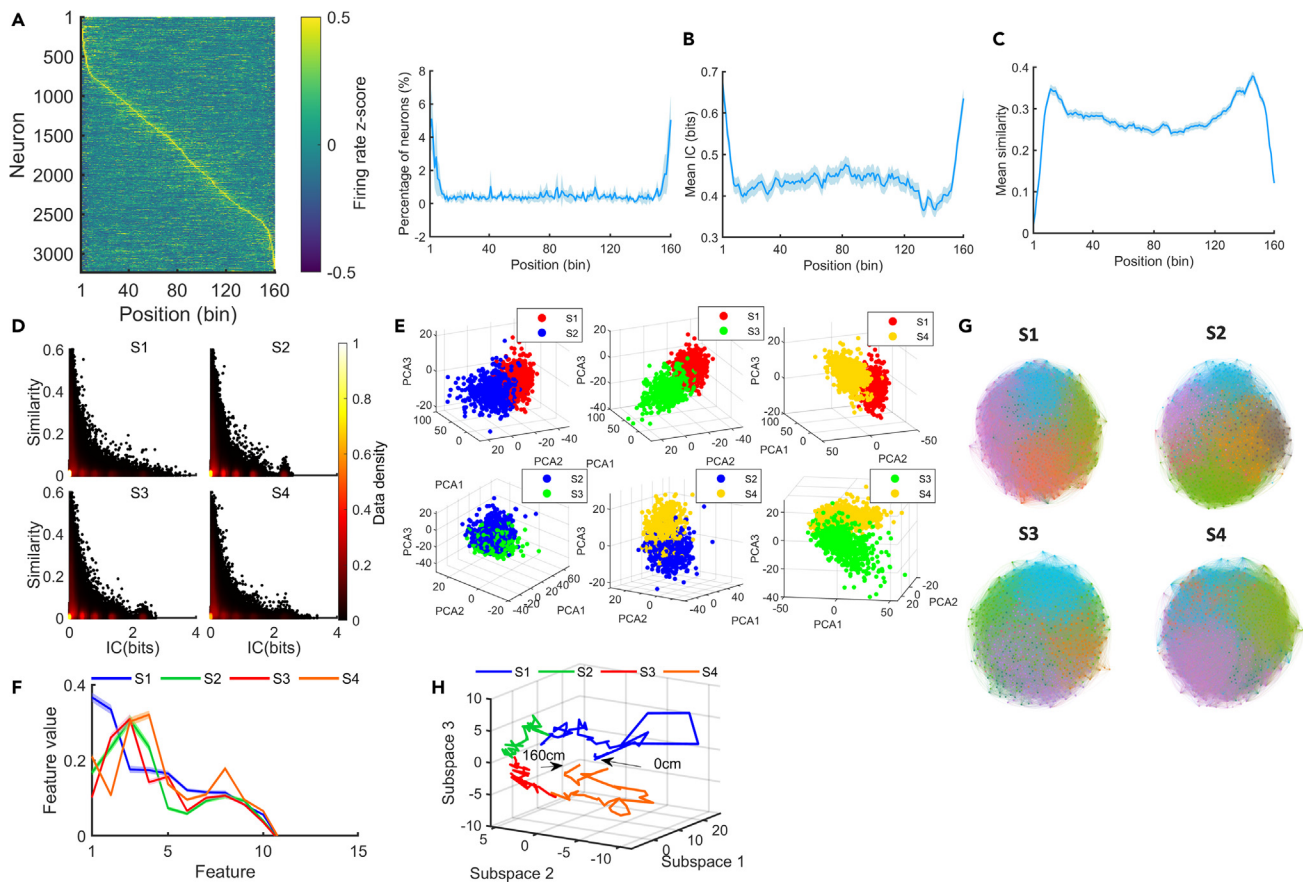


Figure 4. Hippocampal neuronal populations displayed distinct firing patterns in four long spatial segments: spatial bins 1–40 (S1), 41–80 (S2), 81–120 (S3), and 121–160 (S4)

- (A) Hippocampal place field map and the distribution of each neuron's most sensitive location.
 (B) Neurons in S1 and S4 carried higher information content than that in S2 and S3.
 (C) Neuronal firing patterns in S1 and S4 showed high stability across trials when measured using the cosine similarity index.
 (D) Information-similarity joint density distribution showed distinct patterns in different spatial bins.
 (E) Examples of neuronal firing patterns analyzed using an autoencoder. Each dot represents the firing pattern of a specific neuron. PCA was applied to results for better visualization.
 (F) The average features values extracted using the autoencoder.
 (G) Examples of neural network topology graphs in different spatial bins.
 (H) An example of the neural manifolds representation.

neural firing patterns, the autoencoder effectively splits firing patterns into different clusters (Figures 5E, 5F, S13D, and S13E). Neurons showed different sensitivity to stimuli. In contrast to other scenarios, LQ-LS and DQ-DS had fewer reactive neurons (Figure S14), possibly implying intrinsically weaker sensitivity to sound.

We next studied the network topology under mixed stimuli (Figures 5G and S15A–S15E). Although the graph density and each neuron's impact on the network were comparable among the different stimulus patterns, network connectivity was altered. The clustering coefficient of neuronal populations in LQ and LS epochs was substantially higher than that in DQ and DS epochs. Additionally, neurons in LS epochs displayed a more localized connectivity. The neural manifold representing population activity under different stimuli intertwined together after dimensionality reduction, with similar manifold amplitudes. However, the manifold angles showed different temporal patterns (Figures 5H and S15F–S15H). Criticality measures were estimated by dividing the time epochs in half; the system again showed evidence of critical behavior, but all metrics were stable over time. (Figure S16).

DISCUSSION

In this study, we recorded both spatial and non-spatial modality responses in the rodent hippocampus using wide-field imaging of hundreds of neurons. The use of multi-neuronal ensemble recording during multisensory stimulation, in combination with advanced network analysis, has yielded valuable insights into the intricacies of neuronal dynamics and coding patterns within hippocampal circuits, significantly

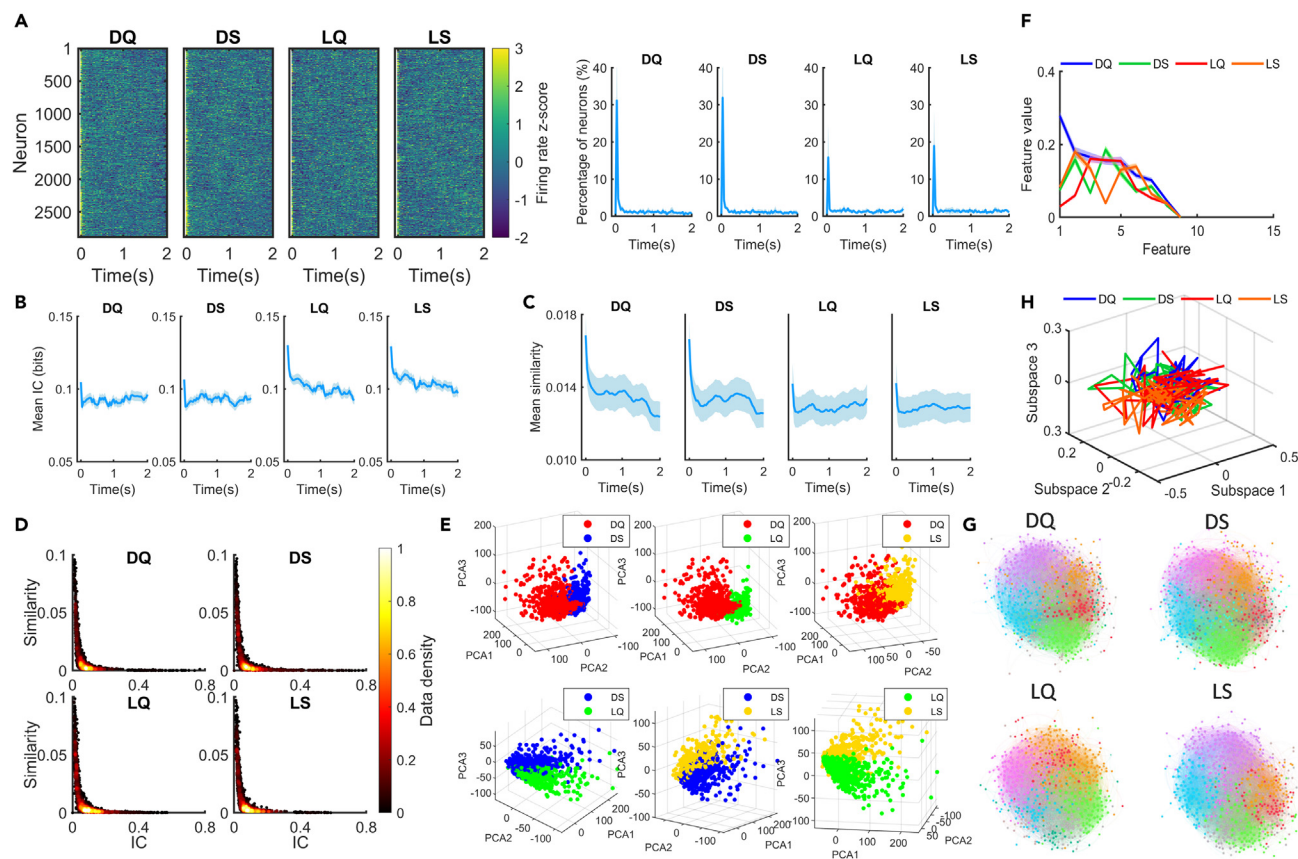


Figure 5. Visual and auditory mixed stimuli evoked distinct neuronal firing patterns in different windows

The brain activity was sectioned into four different types of epochs (DQ: dark + mute; DS: dark + sound; LQ: light + mute; LS: light + sound).

(A) The left figure shows the average neuronal temporal firing rate map over trials when the animal was in different environments. The right figure shows the distribution of neuronal response latencies.

(B–D) (B) Neurons in LQ and LS epochs showed higher information content than that in DQ and DS epochs (C) Neuronal firing patterns in DQ and DS epochs showed high stability across trials than that in LQ and LS epochs when measured using the cosine similarity index (D) Information-similarity joint density distribution showed distinct patterns in different epochs.

(E) Examples of neuronal firing patterns analyzed using an autoencoder. Each dot represents the firing pattern of a specific neuron. PCA was applied to the results for better visualization.

(F) Firing patterns in different windows exhibited different average feature values.

(G) An example of the network topology structures in different window.

(H) An example of the neural manifolds representation.

advancing our understanding of the relational theory and cognitive maps theory. We demonstrate that the hippocampus processes non-spatial information independently of spatial inputs. The network’s topological configuration demonstrates dense interconnections for spatial information while exhibiting sparse connectivity for non-spatial information (Figures 2G, 3G, 4G, and 5G). Furthermore, neuronal populations exhibit distinct coding mechanisms depending on sensory inputs (Figures 2H, 3H, 4H, and 5H). These findings contribute to our understanding of hippocampal neuronal population activity across different information modalities and offer potential support for the relational theory.

The hippocampus is a key structure in the brain that processes spatial information. It is not generally considered a part of the visual or auditory system. However, several pathways for both are well described. Visual inputs are transmitted to the hippocampus through the surrounding neocortex via multi-synaptic pathways.^{13,14} Auditory inputs project from polysensory cortex,¹⁵ then to the hippocampus through a medial septum relay.^{16,17} Thus, visual and auditory signaling to the hippocampus likely undergoes distinct integrative stages that affect neural activity propagation. In contrast to previous work,^{18–20} where neuronal response latencies to visual or auditory stimuli exhibited irregular random distributions, the majority of neurons showed rapid responses in our experiments. This is possibly due to different experimental design as visual or auditory stimuli are coupled with other sensory modalities in previous experiments. For example, previous study recorded responses on a rotating plate and animal movement might have influenced the neural activity.¹⁹

By assessing the information content and cosine similarity index of neuronal firing patterns, we found that CA1 neurons displayed different coding complexity and stability depending on the sensory inputs. Visual and auditory stimuli modulated temporal features of neural activity

differentially. As opposed to auditory information, which was coded over a long period of time, visual information was primarily encoded as stimuli occurred. Additionally, neuronal activity with high information content typically displayed high stability in visual experiments but low stability in auditory experiments (Figures 2B, 2C, 3B, and 3C). In contrast to non-spatial modalities, neural activity was strongly modulated by spatial inputs via more complex but stable processes (Figures 4B and 4C). These differences may be ascribed to the intrinsic properties of hippocampal neurons or due to different information flow pathways. It will be of considerable interest to study the neuronal activity in the major hippocampal input entorhinal cortex, which is increasingly believed to have a perceptual function.²¹

Although some deep neural network-based classifiers allow the classification of patterns with great accuracy, these algorithms require extremely large datasets and are challenging to determine which specific features inform the categorization decision.²² Instead of constructing a classifier, we used an unsupervised autoencoder to extract internal features of the patterns. In all scenarios, patterns could be distinguished even in conditions where the information content and cosine similarity index showed comparable results (Figures 2E, 3E, 4E, and 5E). It is worth noting that the patterns in both spatial and non-spatial experiments can be described using around ten features (Figures 2F, 3F, 4F, and 5F). As multi-sensory experiences are consolidated in the hippocampus,²³ this number may imply intrinsic characteristics of the hippocampal network, like the number of senses. Future model work or BCI applications may benefit from this finding.

Application of graph theory provides a coherent approach to study functional connectivity in a regional network or globally.²⁴ Previous studies pointed out that the hippocampal network in spatial cognition was topological,²⁵ which was supported by the results of current experiments (Figure 4G). Additionally, we found that hippocampal network topology dynamically reconfigured under different conditions in response to various stimuli (Figures 2G, 3G, and 5G). Such reconfiguration may form a fundamental neurophysiological mechanism for cognitive functions as suggested by previous studies.²⁶

Recent findings that rhythmic light flicker can rescue hippocampal low gamma oscillation and improves cognition in Alzheimer's disease mouse models¹¹ suggest an important role of rhythmic stimuli in tuning hippocampal neural activity and the network restructuring observed in the current study may potentially be related to this observation (Figures 2F and 2G). It would be of considerable interest to directly observe the effects of these flicker stimuli on network structure and criticality, as we have recently correlated criticality with cognitive tasks using the same wide-field calcium imaging technique.

It has been hypothesized that population activity in cortical regions is confined in neural manifolds, which are low-dimensional parameter spaces embedded in the original neural state space.²⁷ We observed distinct temporal feature patterns for different types of information, indicating distinct information processing mechanisms. In visual stimuli experiments and linear track experiments, encoding geometries varied smoothly in time, but somewhat abruptly in auditory stimuli experiments (Figures 2H and 3H). An intriguing finding is that manifold activity under different stimuli intertwined in mixed stimulus experiments (Figure 5H), suggesting similar information processing mechanisms in this case, possibly due to the complexity of the stimuli, which might overload the animal's cognitive capacity. Previous study suggests that local regions of neural manifolds could have further substructures related to conditions.²⁸ This hypothesis was validated in our experiments, where different frequencies occupied separate regions in the corresponding neural manifolds (Figure 3H). However, the population activity in mixed stimulus experiments showed certain overlap in neural manifolds (Figure 5H), showing that further studies are needed to define manifold complexity and structure.

Recent studies have attempted to show that neural ensembles display self-organized criticality, especially in the context of potential functional efficiency that may accrue from such regimes.^{29–31} Brain criticality analysis has been applied to a variety of clinically relevant domains such as epilepsy, neurodegenerative disease, anesthesia, and psychiatry.³² It has been suggested as an efficient measurement to study the information processing.³³ Measuring several metrics that are necessary conditions for critical behavior, we found that indeed hippocampal CA1 neuronal ensembles appeared to display critical dynamics, but with varying properties depending on the type of stimuli observed. DCC, SC, and BR are commonly used measurements to quantify the system criticality. The measurements of DCC and SC are both calculated based on power-laws distributions of avalanches properties. In contrast, the BR approach measures the percentage of triggered events among all the events and does not employ the avalanches construct. However, whether branching process like models can reproduce the statistics of spike avalanches remains controversial.³⁴ In visual and auditory stimuli experiments, system dynamics moved away from the critical point as time passed considering increased DCC errors. While BR errors only increased significantly in visual but not in auditory experiments, showing that changes in avalanches properties did not always lead to alterations in branching processes (Figures S4 and S8). Compared with visual and auditory stimuli experiments, the system dynamics did not change in mixed stimuli experiments (Figure S16). This could be attributed to the need for efficient information processing as the stimuli became more complicated in these experiments.

To ensure a substantial number of trial recordings for our analysis, we conducted long-time recordings. However, a significant challenge we encountered was the photobleaching of fluorescent calcium indicators. Consequently, we were able to record 300 trials in visual stimulus experiments, but only 100 trials/frequency in auditory stimulus experiments. Given the substantial difference bias in trial numbers and the variations in stimulus repeat patterns, it may not be suitable to directly compare the results between these two sets of experiments. To address this issue, we conducted a mixed stimuli experiment to compare the responses elicited by visual and auditory stimuli. In this scenario, we had four different background environments. To mitigate photobleaching, we needed to shorten the duration of each trial. Therefore, direct result comparisons with the other two experiments may not be appropriate due to the differences in stimulus patterns. To tackle the photobleaching issue and facilitate result comparisons in future studies, one method is to utilize UCLA miniscope version 4. This updated version incorporates a more sensitive Python CMOS chip and could substantially extend the recording length.

In summary, this study advances our understanding of the hippocampal population activity in response to diverse modalities of information and offers innovative perspectives on the interpretation of relational theory and cognitive maps theory. Our findings demonstrate that

while the CA1 neuronal population primarily processes spatial information, it also exhibits a considerable degree of sensitivity to non-spatial modalities that are independent of spatial inputs. These results provide support for the relational theories.

Limitations of the study

While some cells exhibit non-spatial responses independent of spatial ones, others may display spatial responses independently of non-spatial ones, and some may exhibit combined spatial and non-spatial responses. Thus, the current study only provides support for the relational theory, and we cannot definitively conclude that the cognitive map theory is incorrect. One possible avenue for future research is to explore this by deploying an infrared eye tracking system to accurately detect the animal's spatial input in the chamber.

STAR★METHODS

Detailed methods are provided in the online version of this paper and include the following:

- KEY RESOURCES TABLE
- RESOURCE AVAILABILITY
 - Lead contact
 - Materials availability
 - Data and code availability
- EXPERIMENTAL MODEL AND SUBJECT DETAILS
- METHOD DETAILS
 - Surgery protocols
 - Experimental protocol
 - Calcium activity analysis
 - Information content
 - Cosine similarity index
 - Information-similarity density
 - Neuronal firing pattern extraction
 - Weighted normalized mutual information
 - Neuronal sensitivity to stimuli
 - Network graphs
 - Neural manifolds
 - Criticality analysis
- QUANTIFICATION AND STATISTICAL ANALYSIS

SUPPLEMENTAL INFORMATION

Supplemental information can be found online at <https://doi.org/10.1016/j.isci.2023.108603>.

ACKNOWLEDGMENTS

This work was supported by the Australian Research Council under Discovery Project (DP170100363) and Royal Melbourne Hospital Neuroscience Foundation.

AUTHOR CONTRIBUTIONS

D.S., R.R.U., and C.F. conceived and designed the study. D.S. carried out the experiment, processed the data, and drafted the manuscript. N.E.K.S. processed the data. R.R.U. and C.F. did the critical manuscript revision. All authors have read and approved the final manuscript.

DECLARATION OF INTERESTS

All authors disclose no conflict of interests for this work.

Received: August 21, 2023

Revised: November 6, 2023

Accepted: November 29, 2023

Published: December 1, 2023

REFERENCES

1. Eichenbaum, H., Dudchenko, P., Wood, E., Shapiro, M., and Tanila, H. (1999). The hippocampus, memory, and place cells: is it spatial memory or a memory space? *Neuron* 23, 209–226.
2. Bird, C.M., and Burgess, N. (2008). The hippocampus and memory: insights from spatial processing. *Nat. Rev. Neurosci.* 9, 182–194.
3. Lisman, J., Buzsáki, G., Eichenbaum, H., Nadel, L., Ranganath, C., and Redish, A.D. (2017). Viewpoints: how the hippocampus contributes to memory, navigation and cognition. *Nat. Neurosci.* 20, 1434–1447.
4. O'Keefe, J., and Nadel, L. (1979). *Précis of O'Keefe & Nadel's The hippocampus as a cognitive map*. *Behav. Brain Sci.* 2, 487–494.
5. O'Keefe, J., and Krupic, J. (2021). Do hippocampal pyramidal cells respond to nonspatial stimuli? *Physiol. Rev.* 101, 1427–1456.
6. Aronov, D., Nevers, R., and Tank, D.W. (2017). Mapping of a non-spatial dimension by the hippocampal-entorhinal circuit. *Nature* 543, 719–722.
7. Behrens, T.E.J., Muller, T.H., Whittington, J.C.R., Mark, S., Baram, A.B., Stachenfeld, K.L., and Kurth-Nelson, Z. (2018). What is a cognitive map? Organizing knowledge for flexible behavior. *Neuron* 100, 490–509.
8. Montijn, J.S., Meijer, G.T., Lansink, C.S., and Pennartz, C.M.A. (2016). Population-level neural codes are robust to single-neuron variability from a multidimensional coding perspective. *Cell Rep.* 16, 2486–2498.
9. Stringer, C., Pachitariu, M., Steinmetz, N., Reddy, C.B., Carandini, M., and Harris, K.D. (2019). Spontaneous behaviors drive multidimensional, brainwide activity. *Science* 364, 255.
10. Scharwächter, L., Schmitt, F.J., Pallast, N., Fink, G.R., and Aswendt, M. (2022). Network analysis of neuroimaging in mice. *Neuroimage* 253, 119110.
11. Zheng, L., Yu, M., Lin, R., Wang, Y., Zhuo, Z., Cheng, N., Wang, M., Tang, Y., Wang, L., and Hou, S.-T. (2020). Rhythmic light flicker rescues hippocampal low gamma and protects ischemic neurons by enhancing presynaptic plasticity. *Nat. Commun.* 11, 3012.
12. Ghosh, K.K., Burns, L.D., Cocker, E.D., Nimmerjahn, A., Ziv, Y., Gamal, A.E., and Schnitzer, M.J. (2011). Miniaturized integration of a fluorescence microscope. *Nat. Methods* 8, 871–878.
13. Lavenex, P., and Amaral, D.G. (2000). Hippocampal-neocortical interaction: A hierarchy of associativity. *Hippocampus* 10, 420–430.
14. Ranganath, C., and Ritchey, M. (2012). Two cortical systems for memory-guided behaviour. *Nat. Rev. Neurosci.* 13, 713–726.
15. Zhang, L., Wang, J., Sun, H., Feng, G., and Gao, Z. (2022). Interactions between the hippocampus and the auditory pathway. *Neurobiol. Learn. Mem.* 189, 107589.
16. Vinogradova, O. (1975). Functional organization of the limbic system in the process of registration of information: facts and hypotheses. In *The Hippocampus: Volume 2: Neurophysiology and Behavior* (Springer), pp. 3–69.
17. Kaifosh, P., Lovett-Barron, M., Turi, G.F., Reardon, T.R., and Losonczy, A. (2013). Septo-hippocampal GABAergic signaling across multiple modalities in awake mice. *Nat. Neurosci.* 16, 1182–1184.
18. Itskov, P.M., Vinnik, E., Honey, C., Schnupp, J., and Diamond, M.E. (2012). Sound sensitivity of neurons in rat hippocampus during performance of a sound-guided task. *J. Neurophysiol.* 107, 1822–1834.
19. Liu, Y.z., Wang, Y., Tang, W., Zhu, J.y., and Wang, Z. (2018). NMDA receptor-gated visual responses in hippocampal CA1 neurons. *J. Physiol.* 596, 1965–1979.
20. Xiao, C., Liu, Y., Xu, J., Gan, X., and Xiao, Z. (2018). Septal and hippocampal neurons contribute to auditory relay and fear conditioning. *Front. Cell. Neurosci.* 12, 102.
21. Baxter, M.G. (2009). Involvement of medial temporal lobe structures in memory and perception. *Neuron* 61, 667–677.
22. Zhang, Y., Tiño, P., Leonardis, A., and Tang, K. (2021). A survey on neural network interpretability. *IEEE Trans. Emerg. Top. Comput. Intell.* 5, 726–742.
23. Fortin, N.J., Agster, K.L., and Eichenbaum, H.B. (2002). Critical role of the hippocampus in memory for sequences of events. *Nat. Neurosci.* 5, 458–462.
24. Gonzalez, W.G., Zhang, H., Harutyunyan, A., and Lois, C. (2019). Persistence of neuronal representations through time and damage in the hippocampus. *Science* 365, 821–825.
25. Dabaghian, Y., Brandt, V.L., and Frank, L.M. (2014). Reconciling the hippocampal map as a topological template. *Elife* 3, e03476.
26. Braun, U., Schäfer, A., Walter, H., Erk, S., Romanczuk-Seifert, N., Haddad, L., Schweiger, J.I., Grimm, O., Heinz, A., Tost, H., et al. (2015). Dynamic reconfiguration of frontal brain networks during executive cognition in humans. *Proc. Natl. Acad. Sci. USA* 112, 11678–11683.
27. Ebitz, R.B., and Hayden, B.Y. (2021). The population doctrine in cognitive neuroscience. *Neuron* 109, 3055–3068.
28. Koay, S.A., Charles, A.S., Thiberge, S.Y., Brody, C.D., and Tank, D.W. (2022). Sequential and efficient neural-population coding of complex task information. *Neuron* 110, 328–349.e11.
29. De Arcangelis, L., Perrone-Capano, C., and Herrmann, H.J. (2006). Self-organized criticality model for brain plasticity. *Phys. Rev. Lett.* 96, 028107.
30. Chialvo, D.R. (2010). Emergent complex neural dynamics. *Nat. Phys.* 6, 744–750.
31. Cocchi, L., Gollo, L.L., Zalesky, A., and Breakspear, M. (2017). Criticality in the brain: A synthesis of neurobiology, models and cognition. *Prog. Neurobiol.* 158, 132–152.
32. Zimmern, V. (2020). Why brain criticality is clinically relevant: a scoping review. *Front. Neural Circ.* 14, 54.
33. O'Byrne, J., and Jerbi, K. (2022). How critical is brain criticality? *Trends Neurosci.* 45, 820–837.
34. Ribeiro, T.L., Ribeiro, S., Belchior, H., Caixeta, F., and Copelli, M. (2014). Undersampled critical branching processes on small-world and random networks fail to reproduce the statistics of spike avalanches. *PLoS One* 9, e94992.
35. Ehret, G., and Riecke, S. (2002). Mice and humans perceive multiharmonic communication sounds in the same way. *Proc. Natl. Acad. Sci. USA* 99, 479–482.
36. Sun, D., Unnithan, R.R., and French, C. (2021). Scopamine impairs spatial information recorded with “miniscope” calcium imaging in hippocampal place cells. *Front. Neurosci.* 15, 640350.
37. Pnevmatikakis, E.A., and Giovannucci, A. (2017). NoRMCorre: An online algorithm for piecewise rigid motion correction of calcium imaging data. *J. Neurosci. Methods* 291, 83–94.
38. Zhou, P., Resendez, S.L., Rodriguez-Romaguera, J., Jimenez, J.C., Neufeld, S.Q., Giovannucci, A., Friedrich, J., Pnevmatikakis, E.A., Stuber, G.D., Hen, R., et al. (2018). Efficient and accurate extraction of *in vivo* calcium signals from microendoscopic video data. *Elife* 7, e28728.
39. Friedrich, J., Zhou, P., and Paninski, L. (2017). Fast online deconvolution of calcium imaging data. *PLoS Comput. Biol.* 13, e1005423.
40. Shuman, T., Aharoni, D., Cai, D.J., Lee, C.R., Chavlis, S., Page-Harley, L., Vetere, L.M., Feng, Y., Yang, C.Y., Mollinedo-Gajate, I., et al. (2020). Breakdown of spatial coding and interneuron synchronization in epileptic mice. *Nat. Neurosci.* 23, 229–238.
41. Ravassard, P., Kees, A., Willers, B., Ho, D., Aharoni, D.A., Cushman, J., Aghajian, Z.M., and Mehta, M.R. (2013). Multisensory control of hippocampal spatiotemporal selectivity. *Science* 340, 1342–1346.
42. Carrillo-Reid, L., Miller, J.-E.K., Hamm, J.P., Jackson, J., and Yuste, R. (2015). Endogenous sequential cortical activity evoked by visual stimuli. *J. Neurosci.* 35, 8813–8828.
43. Kramer, M.A. (1991). Nonlinear principal component analysis using autoassociative neural networks. *AIChE J.* 37, 233–243.
44. Pang, B., Nijkamp, E., and Wu, Y.N. (2020). Deep learning with tensorflow: A review. *J. Educ. Behav. Stat.* 45, 227–248.
45. Estévez, P.A., Tesmer, M., Perez, C.A., and Zurada, J.M. (2009). Normalized mutual information feature selection. *IEEE Trans. Neural Network.* 20, 189–201.
46. Kruschwitz, J.D., List, D., Waller, L., Rubinov, M., and Walter, H. (2015). GraphVar: a user-friendly toolbox for comprehensive graph analyses of functional brain connectivity. *J. Neurosci. Methods* 245, 107–115.
47. Newman, M.E.J. (2003). The structure and function of complex networks. *SIAM Rev.* 45, 167–256.
48. Blondel, V.D., Guillaume, J.-L., Lambiotte, R., and Lefebvre, E. (2008). Fast unfolding of communities in large networks. *J. Stat. Mech. Theor. Exp.* 2008, P10008.
49. Ruhnau, B. (2000). Eigenvector-centrality—a node-centrality? *Soc. Network.* 22, 357–365.
50. Jacomy, M., Venturini, T., Heymann, S., and Bastian, M. (2014). ForceAtlas2, a continuous graph layout algorithm for handy network visualization designed for the Gephi software. *PLoS One* 9, e98679.
51. Chung, S., and Abbott, L.F. (2021). Neural population geometry: An approach for understanding biological and artificial neural networks. *Curr. Opin. Neurobiol.* 70, 137–144.
52. Beggs, J.M., and Timme, N. (2012). Being critical of criticality in the brain. *Front. Physiol.* 3, 163.

53. Friedman, N., Ito, S., Brinkman, B.A.W., Shimono, M., DeVille, R.E.L., Dahmen, K.A., Beggs, J.M., and Butler, T.C. (2012). Universal critical dynamics in high resolution neuronal avalanche data. *Phys. Rev. Lett.* *108*, 208102.
54. Poil, S.-S., Hardstone, R., Mansvelder, H.D., and Linkenkaer-Hansen, K. (2012). Critical-state dynamics of avalanches and oscillations jointly emerge from balanced excitation/inhibition in neuronal networks. *J. Neurosci.* *32*, 9817–9823.
55. Marshall, N., Timme, N.M., Bennett, N., Ripp, M., Lautzenhiser, E., and Beggs, J.M. (2016). Analysis of power laws, shape collapses, and neural complexity: new techniques and MATLAB support via the NCC toolbox. *Front. Physiol.* *7*, 250.
56. Ma, Z., Turrigiano, G.G., Wessel, R., and Hengen, K.B. (2019). Cortical circuit dynamics are homeostatically tuned to criticality *in vivo*. *Neuron* *104*, 655–664.e4.
57. Wilting, J., and Priesemann, V. (2018). Inferring collective dynamical states from widely unobserved systems. *Nat. Commun.* *9*, 2325.

STAR★METHODS

KEY RESOURCES TABLE

REAGENT or RESOURCE	SOURCE	IDENTIFIER
Bacterial and virus strains		
pAAV.Syn.GCaMP6f.WPRE.SV40	Addgene	100837
Chemicals, peptides, and recombinant proteins		
Isoflurane	VET ONE	502017
Carprofen	Rimadyl	Small Animal Solution for Injection
Dexamethasone	Sigma-Aldrich	D4902
Enrofloxacin	Baytril	Baytril 2.5%
Experimental models: Organisms/strains		
Male C57BL/6J mice	Australia Resources Center	N/A
Software and algorithms		
Matlab 2019a	Mathworks	http://www.mathworks.com
Graphpad Prism 9	Graphpad	https://www.graphpad.com/
CNMF-E	https://github.com/zhoup/cnmf_e	N/A
NormCorre	https://github.com/flatironinstitute/NoRMCorre	N/A
Calcium signal deconvolution algorithm	https://github.com/j-friedrich/OASIS	N/A
Python 3.7	Python Software Foundation	https://www.python.org/
Other		
Grin lens	Edmund Optics	64-519
Miniscope	UCLA Miniscope	http://miniscope.org
Torch	Jaycar	ST3481
Speaker	Jaycar	XC3744
Raspberry Pi 3	Raspberry Pi	https://www.raspberrypi.com/products/raspberry-pi-3-model-b/

RESOURCE AVAILABILITY

Lead contact

Further information and requests for resources and reagents should be directed to and will be fulfilled by the lead contact, Dr. Chris French (frenchc@unimelb.edu.au).

Materials availability

This study did not generate new unique reagents.

Data and code availability

- All data reported in this paper will be shared by the [lead contact](#) upon request.
- This paper does not report original code. All custom MATLAB scripts will be available upon request.
- Any additional information required to reanalyze the data reported in this work paper is available from the [lead contact](#) upon request.

EXPERIMENTAL MODEL AND SUBJECT DETAILS

All procedures were carried out in accordance with the Australian Animal Welfare Committee guidelines and approved by Florey Animal Ethics Committee (No. 18-008UM). Male C57BL/6 mice (aged 10–12 weeks, 23-25g) were maintained on a 12-hour light/dark cycle with water and standard mice chow *ad libitum*.

METHOD DETAILS

Surgery protocols

We first injected 500nl of pAAV.Syn.GCaMP6f.WPRE.SV40 virus (viral load: 2.2×10^{13} GC/mL; AddGene, USA) into dorsal hippocampus (coordinates: AP -2.1mm, ML +2.1mm, DV -1.7mm). The injection speed was less than 35 nl/min and the injector was left in place for extra 10 minutes to allow for viral diffusion. One week after viral transduction, a round craniotomy (diameter: 2mm) was made at -2.1mm posterior and 1.6mm right of bregma. Overlying brain tissue was aspirated to expose hippocampal vertical striations with a 27-gauge blunt needle and artificial cerebrospinal fluid was applied to provide a clear operating field. A grin lens (0.23 pitch, No. 64-519, Edmund Optics) was lowered to the bottom of the craniotomy (-1.35mm from the top of the skull) and secured with cyanoacrylate. Two M1 anchor screws were fixed close to the lens (coordinates: AP +1.8, ML -2.5; AP -2.8, ML -0.8) and dental acrylic was built around the lens for support. Carprofen (5mg/kg), dexamethasone (0.5 mg/kg), and enrofloxacin water were injected after the surgery and provided to the animal daily for one week. Five weeks following the implantation surgery, neurons were observed using a miniscope with a baseplate attached at the bottom. Upon finding an optimal position for imaging, the baseplate was mounted on the head cap with dental acrylic, and the focal length adjustment screw was tightened in place (Figure 1A). Throughout the experiment, we encountered challenges such as animal mortality, headpiece detachment, and signal loss. Thus, different mice were used in each experiment.

Experimental protocol

On the day of the experiment, the experimental animal was brought into a silent room 30 minutes prior to the beginning of the recording to acclimate to the new environment and the miniscope was attached with optimized LED excitation intensity.

In the linear track experiment, trained mice traversed a 1.6m linear track for 16 running trials, and neural activity recorded. A camera fixed overhead was synchronized with the miniscope to track the animal's location. In light stimulus experiments, an LED light source was mounted above the chamber and the luminance was set at 380 lux. Previous work¹⁹ found that neuronal populations exhibited widely distributed response latencies to stimuli, with a maximum around 2 seconds. Consequently, we selected a 2-second stimulus duration and employed a 3-second interval to minimize any significant influence of the previous epoch's stimulus on the current epoch's neuronal responses. The light source was activated (2s) and deactivated (3-3.5s) alternately 300 times. With sound stimuli, a speaker was fixed on top of the chamber and the intensity was set at 70 dB SPL, providing three pure sinusoidal tones centred at 4kHz, 8kHz, and 16kHz, lying within both human and mouse hearing sensitivity ranges and including the most sensitive frequencies in the mouse audiogram.³⁵ The auditory stimuli were activated (2s) and deactivated (3-3.5s) alternately in a random order with the stimulus at each frequency repeated 100 times. With light-sound mixed stimuli, the visual and auditory stimuli (pure sinusoidal tone centred at 8kHz) were combined. In total, four different background environments (dark + silent; dark + sound; light + silent; light + sound) in a random order were used. Each environment was 2s in duration and repeated 200 times. The light source and speaker were controlled and synchronized with the miniscope by a Raspberry Pi 3 board with custom-designed software (Figure 1B). A summary of the stimuli pattern is provided in Table S1.

Calcium activity analysis

The analysis pipelines were similar to our previous reports.³⁶ Briefly, a non-rigid motion correction algorithm was applied first to register the raw images.³⁷ Next, a constrained non-Negative Matrix Factorization for Endoscopic recordings algorithm (CNMF-E) was used to extract neural calcium activity.³⁸ The calcium activity of each neuron was deconvolved using a pool adjacent violators algorithm.³⁹ An example of the deconvolved neural activity is shown in Figure 1A. Finally, the temporal neural activity was binarized to obtain the temporal calcium events.⁴⁰ In the linear track experiment, the data on each end of the track was excluded from the analysis.

Information content

Information content⁴¹ measures the coding complexity of each neuron, and a larger value indicates higher complexity. In the linear track experiment, the data was divided into 1 cm spatial bins for analysis. In stimuli experiments, the binning method was converted from spatial domain to temporal domain ($\text{bin}=1/F_s$, where the sampling frequency $F_s=30$ frame/second). The information content is defined as:

$$I = \sum_{i=1}^K P_i \frac{\lambda_i}{\bar{\lambda}} \log_2 \frac{\lambda_i}{\bar{\lambda}}$$
$$\bar{\lambda} = \sum_{i=1}^K P_i \lambda_i$$

where K represents the number of spatial bins (linear track experiment) or the length of the epoch data (stimuli experiments), P_i is the occupancy ratio of the i -th bin, λ_i is the neural calcium event rate in the i -th bin, $\bar{\lambda}$ is the mean calcium event rate.

Cosine similarity index

A "cosine similarity index" between individual neurons was used to quantify the stability of neuronal firing patterns. The similarity of each neuron was defined as the normalized inner product of the activity between every two running trials or stimuli epochs,⁴²

$$S = \frac{1}{N(N-1)} \sum_{i=1}^{N-1} \sum_{j=i+1}^N \frac{2 \cdot C_i C_j}{(C_i^2 + C_j^2)}$$

where S represents cosine similarity index, N represents the total number of running trials or stimuli epochs, C_i and C_j are neural calcium event vectors in the i -th and j -th trials or epochs. This metric is restricted to $[0, 1]$, where “1” means the neuronal firing patterns are the same in all trials or epochs, while “0” means they are completely different.

Information-similarity density

We introduce a new measure called “information-similarity density” to calculate the density distribution of the information content and cosine similarity index measured on each neuron within a surrounding ellipse area. The boundary of the ellipse is defined as:

$$\left(\frac{x - x_0}{a}\right)^2 + \left(\frac{y - y_0}{b}\right)^2 < 1$$

$$a = \frac{x_{max} - x_{min}}{100}, b = \frac{y_{max} - y_{min}}{100}$$

where x and y represent the information content and cosine similarity index, x_0 and y_0 represent the centre of the ellipse. The boundary of the ellipse is limited to a small region to increase the resolution, where the half-length of the ellipse major axis (a), and minor axis (b) are set to be one percent of the information content range ($x_{max} - x_{min}$) and cosine similarity index range ($y_{max} - y_{min}$).

Neuronal firing pattern extraction

The information content and cosine similarity index are two metrics that quantify differences in neural firing patterns, but they may fail to detect non-obvious differences in some cases (see Results). We used an autoencoder to detect differences in neuronal firing patterns under different contexts in a high dimensional parameter space. An autoencoder is a type of unsupervised artificial neural network that learns to copy its input to its output through layers with fewer neurons, providing useful dimensionality reduction of complex data spaces.⁴³ It combines two parts: encoder and decoder. The encoder decreases the dimensionality of data, and the decoder learns to reconstruct the original input. During training, the encoder identifies the most significant components from the original data. We constructed an autoencoder using the Tensorflow machine learning platform⁴⁴ to decrease the dimensionality of the neural calcium events epoch data. The inputs of the model were the spatial firing rates of each neuron in the running trials or temporal firing rates in each epoch. Both the encoder and decoder were constructed with three dense layers and scaled exponential linear unit (SELU) activation functions. A binary cross entropy loss function and an Adam optimizer were chosen to train the model and a grid search method fitted the parameters including learning rate, the number of nodes in each layer, and the number of training epochs to minimize the reconstructed data error.³⁶ Given the substantial workload involved in optimizing parameters using datasets from five animals in four different experiments, we chose not to conduct a comprehensive grid search for hyperparameter optimization. We began by identifying and tuning the most impactful hyperparameters while keeping others at reasonable values. The testing values for the grid search were determined based on previous experience and some random testing. The mean reconstruction error was found to be $3.84\% \pm 1.60\%$ in visual stimuli experiments, $4.91\% \pm 1.87\%$ in auditory stimuli experiments, $5.37\% \pm 1.93\%$ in linear track experiments, and $5.28\% \pm 1.85\%$ in mixed stimuli experiments. In the encoder, we found that a configuration of 1200 nodes in the first dense layer, 120 nodes in the second dense layer, and 15 nodes in the third dense layer was a typical good choice for achieving satisfactory reconstruction. In the decoder, the number of nodes in each dense layer is reversed, with 15 nodes in the first dense layer, 120 in the second, and 1200 in the third. As these features were described in a high-dimensional space (>3 dimensions), they couldn't be easily visualized. Consequently, we performed Principal Component Analysis (PCA) solely for visualization purposes. Following the feature extraction with the autoencoder, we calculated the cluster distance based on these high-dimensional features. This analysis aimed to assess whether firing patterns under different scenarios could be effectively separated. The distance of two clusters was defined as L2-Norm of centroids calculated using a K-means clustering algorithm.

Weighted normalized mutual information

“Mutual information” is a measure of mutual dependence between variables. Weighted normalized mutual information (WNMI) considers the weights of the deconvolved neural activity and adds a normalization term, which is used to detect reactive neurons in response to the various stimulus contexts. Mutual Information yields values from 0 to $+\infty$ and may introduce different levels of bias depending on the datasets. Normalization restricts its values to the range $[0, 1]$ and compensates for the bias towards multivalued features.⁴⁵ The amplitude of calcium events deconvolved from analysis pipelines can be interpreted as the probability that a neuron fires at each frame.

Weighted normalized mutual Information (WNMI) is defined as

$$I_{WN}(X, Y) = \frac{I_W(X, Y)}{\min(U_{WX}(X, Y), U_{WY}(X, Y))}$$

$$I_W(X, Y) = \sum_{y \in Y} \sum_{x \in X} W(y) P(x, y) \log_2 \left[\frac{P(x, y)}{P(x)P(y)} \right]$$

$$W(y) = \frac{1}{1 + e^{-[f(y) - u]}}$$

$$U_{WX}(X, Y) = \sum_{y \in Y} \sum_{x \in X} W(y) P(x, y) \left\{ -\log_2[P(x)] - 1 + \frac{P(x)P(y)}{P(x, y)} \right\}$$

$$U_{WY}(X, Y) = \sum_{y \in Y} \sum_{x \in X} W(y) P(x, y) \left\{ -\log_2[P(x)] - 1 + \frac{P(x)P(y)}{P(x, y)} \right\}$$

where X represents different stimuli scenarios or spatial locations, Y represents firing rates of the calcium events, $I_{WN}(X, Y)$ and $I_W(X, Y)$ are the weighted normalized mutual information and weighted mutual information between X and Y , respectively, and $U_{WX}(X, Y)$ and $U_{WY}(X, Y)$ are normalization terms that represent weighted entropy of variables X and Y . $W(y)$ is the weighting component that takes the form of a logistic function, where $f(y)$ is the amplitude of the neural activity at each time frame that represents the neuronal firing probability and u is the mean amplitude. $P(x, y)$, $P(x)$, and $P(y)$ represent the joint probability density function and probability density functions of X and Y respectively.

Neuronal sensitivity to stimuli

We first measured the weighted normalized mutual Information (WNMI) when comparing the activity between every two stimuli or spatial locations for each neuron. Then the temporal or spatial neural calcium events were shuffled 500 times and the average WNMI was evaluated for each shuffle. For a neuron to be classified as a reactive, the average WNMI must be above chance ($p < 0.05$) with respect to the permutation results.^{18,40}

Network graphs

We quantified patterns of neural population activity of different experimental scenarios using network graphs. This analysis detects non-obvious patterns of neuronal ensemble topological and dynamical responses to various forms of perturbation. We measured the pairwise Pearson correlation between all neuronal activities and set the absolute correlation value (threshold: 0.05) as the edge weight between two neurons in the network graph. One issue with this method is that it can yield negative correlation values, which can be challenging to interpret. In previous studies, two methods have been employed to handle negative values. One approach involves using absolute values, while the other entails setting negative weights to zero.⁴⁶ Both methods have their limitations. The former focuses only on the magnitude of the negative weights, while the latter considers only their sign. In our experiment, we observed a substantial number of negative correlation values, leading us to take the absolute value of correlation coefficients just before applying thresholding. Regarding the choice of the correlation value threshold, there is no consensus within the scientific community on how to select specific thresholds. Using a lower threshold has the advantage of retaining all information, which can be important in certain applications. However, this may result in the inclusion of many noisy or irrelevant connections in the analysis, potentially diluting meaningful relationships. One approach to partially address this issue is to use the correlation value as the edge weight. Assigning weighted edges provides a means to assess the importance of connections within the graph, enabling a more nuanced analysis. In our analysis, we used weighed edges in the graph and opted for a relatively low threshold of 0.05. We refrained from using lower values due to the extremely extended Markov diffusion time. This parameter is directly proportional to the number of random walks required for a walker to diffuse out of a cell group. We measured several fundamental network properties, graph density, clustering coefficient, cell group connectivity, and eigenvector centrality.

The graph density is the proportion of edges present in a graph divided by the maximum possible edges and indicates the ratio of possible relationships in the network that are actually present. The clustering coefficient measures the degree to which nodes in a graph tend to cluster together. It is defined as the number of triangles in the network divided by the number of connected triples of vertices.⁴⁷ Cell groups are detected by evaluating modularity, a measure that quantifies the network's division strength.⁴⁸ The cell group connectivity measures the connectivity of different cell groups. It is defined as the number of edges a node connects with its own cell group divided by all edges it connects with other neurons, and a high value indicates more localized connectivity. Eigenvector centrality⁴⁹ measures the transitive influence of a node in a network while taking into account the influence of neighbours. A node with few connections can have a very high eigenvector centrality score if those connections are to very well-connected others. It is defined as:

$$c(v_i) = \sum_{j=1}^n a_{ij} c(v_j), \quad A c = \lambda c$$

where n is the number of neighbours of the node v_i , $A = a_{ij}$ is the adjacency matrix generated by measuring the pairwise Pearson correlation, λ is the eigenvalue. The centrality scores are normalized such that the sum of all scores equals to 1.

The network graph parameters are presented using ForceAtlas2 layout.⁵⁰ Each node in the graph represents a neuron, and colours represent different cell groups. The size of each node is determined by the value of eigenvector centrality.

Neural manifolds

Several cortical neuronal populations share fundamental mechanisms or principles governing cortical processing, showing similar patterns of activity. Geometrical analysis of neural population activity has led to the identification of topologically defined state spaces termed “neural manifolds” with reduced dimensionality. It is thought that manifolds may better identify dynamically and computationally significant functional structures.⁵¹ To project the population activity from a high dimensional neural state space to low dimensional neural manifolds, we employed an autoencoder for dimensionality reduction. The structure of the autoencoder was similar to the one used in neuronal firing pattern extraction mentioned above with the same optimization method, but the inputs of the model were the neural activity of all neurons at each time point. The outputs from the encoder defined the features/subspaces describing the manifold activity and were used for manifold analysis. The extracted features indicated whether the neuronal population adapts its neural representations in response to external information, such as stimuli. If the population activity at two different time points has similar feature values, this means that the network represents similar information, and vice versa. Furthermore, these features can demonstrate differences in information processing mechanisms for various types of information. We also calculated the Euclidean norm of each temporal vector and the Euclidean angle between each vector with respect to the first temporal vector in manifolds. Manifold amplitudes and angles provide two ways to quantify the similarity between neural modes and indicating when self-similarity changes. This angular analysis is a valuable tool to observe shifts in neural activity patterns over time. When the angle between two vectors is large, it indicates dissimilar population activity patterns at those two time points.

Criticality analysis

Criticality denotes a mode of population activity between states of order and chaos, and it has been proposed that neural population activity with critical dynamics are optimised for information processing and memory capacity. It is still unclear how to determine whether a system is in a critical state or not. While meeting the power-law distribution is a basic requirement, recent literature suggests testing additional metrics.³³ We separately evaluated and compared dynamic states of population activity in the first half and the second half of the different experimental scenarios using four metrics: (1) power-law distributions of the size (S) and duration (D) of neuronal avalanches; (2) Deviation from criticality coefficient (DCC); (3) Shape collapse error (SC error); (4) Branching ratio (BR).

Recent studies have revealed that neuronal populations can generate activity avalanches (a cascade of bursts of activity) with size and duration described by a power-law distribution.^{52,53} We first obtained the “population activity” as the sum of all detected calcium events within each time bin. The neuronal avalanches were detected using a threshold method (>60% of median population activity),⁵⁴ where an avalanche began when the population activity crossed the threshold from below and terminated when it reached the threshold from above. Then, the avalanche size (number of total calcium events) and duration (number of time bins) distributions were fitted with a truncated power-law using a maximum likelihood estimation method⁵⁵:

$$f(x) = A(\mu, x_{min}, x_{max}) x^{-\mu}$$

$$A(\mu, x_{min}, x_{max}) = \frac{1}{\sum_{x=x_{min}}^{x_{max}} x^{-\mu}}$$

where x represents avalanche size or duration; $f(x)$ is the probability mass function; A is a normalized constant; μ represents the power-law exponent τ (avalanche size) or α (avalanche duration).

The deviation from criticality coefficient (DCC) is a measure of how close a system operates to criticality.⁵⁶ As avalanche size scales with the average duration in a critical system according to $\langle S \rangle = D^\beta$, DCC is defined as the absolute difference between estimated $\beta = (\alpha - 1) / (\tau - 1)$ and fitted β , and a smaller DCC value the closer the system is to criticality.⁵³

When a neural system operates in a critical regime, the profiles of avalanches with different durations should have the same scaled mean shape⁵³:

$$s(t, D) \propto D^\gamma F\left(\frac{t}{D}\right)$$

$$F\left(\frac{t}{D}\right) = \left\langle \frac{s(t, D)}{D^\gamma} \right\rangle$$

where $s(t, D)$ represents the number of calcium events at time t given avalanche duration of D ; $\gamma = \beta - 1$; $F\left(\frac{t}{D}\right)$ represents avalanche temporal profiles. A collection of temporal profiles $F\left(\frac{t}{D}\right)$ can be extracted given different duration D , and the proximity to a predicted scaled mean shape can be measured by the shape collapse error (SC error), which is calculated as $\text{var}(F) / (\max(F) - \min(F))^2$.

The branching ratio quantifies the proportion of events at time $t+1$ to those at time t , and a critical system is expected to have a branching ratio equal to 1. We utilized a multiple linear regression-based method⁵⁷ to get an unbiased estimation of the branching ratio:

$$\langle N(t+1) | N(t) \rangle = mN(t) + h$$

$$\langle n(t) | N(t) \rangle = \mu N(t) + \epsilon$$

$$m^k = m_k \sqrt{\frac{\mu^2 \text{var}(N(t))}{\text{var}(n(t))}}$$

where $N(t)$ is the real activity and $n(t)$ is the subsampled activity; m is the branching ratio; h represents external stimuli; μ and ϵ are constants; m_k is the multiple linear regression coefficient of the subsampled activity between time t and $t + k$.

QUANTIFICATION AND STATISTICAL ANALYSIS

Statistical analyses were performed using GraphPad Prism software. The level of significance was set at $p < 0.05$. Statistical significance was assessed by two-tailed paired Student's t -test or one-way repeated-measures analysis of variance (ANOVA) with Bonferroni post-hoc comparisons. Normality of the data was confirmed by Kolmogorov–Smirnov and Shapiro-Wilks test. All results are shown as mean \pm standard error of the mean (SEM).